Detailed Observations of Wind Turbine Clutter with Scanning Weather Radars

B. M. ISOM

School of Electrical and Computer Engineering, and Atmospheric Radar Research Center, University of Oklahoma, Norman, Oklahoma

R. D. PALMER

School of Meteorology, and Atmospheric Radar Research Center, University of Oklahoma, Norman, Oklahoma

G. S. SECREST

NOAA/NWS/NEXRAD Radar Operations Center, Norman, Oklahoma

R. D. RHOTON

Wyle Information Systems Inc., Norman, Oklahoma

D. SAXION, T. L. ALLMON, J. REED, T. CRUM, AND R. VOGT

NOAA/NWS/NEXRAD Radar Operations Center, Norman, Oklahoma

(Manuscript received 10 March 2008, in final form 21 October 2008)

ABSTRACT

The wind power industry has seen tremendous growth over the past decade and with it has come the need for clutter mitigation techniques for nearby radar systems. Wind turbines can impart upon these radars a unique type of interference that is not removed with conventional clutter-filtering methods. Time series data from Weather Surveillance Radar-1988 Doppler (WSR-88D) stations near wind farms were collected and spectral analysis was used to investigate the detailed characteristics of wind turbine clutter. Techniques to mask wind turbine clutter were developed that utilize multiquadric interpolation in two and three dimensions and can be applied to both the spectral moments and spectral components. In an effort to improve performance, a nowcasting algorithm was incorporated into the interpolation scheme via a least mean squares criterion. The masking techniques described in this paper will be shown to reduce the impact of wind turbine clutter on weather radar systems at the expense of spatial resolution.

1. Introduction

The rising cost of oil and the now-accepted threat of human-driven global climate change have paved the way for many alternative, so-called green technologies; one of the fastest growing being wind-generated power. Between 2002 and 2006, the total wind power capacity within the United States has grown by 2.5 times to 11 119 MW (Department of Energy 2007a). The increase in capacity can be attributed to both the technological advances that have reduced the cost of wind turbine production as well as new government tax initiatives that provide incentives for power companies to extend themselves toward green technologies (Department of Energy 2007a,b). As the production costs have decreased, it has become feasible to not only produce larger turbines, but also to construct ever larger collections of turbines called wind farms (Department of Energy 2007c). Ideal locations for wind farms and the arrangement of the turbines within the farm are determined after extensive climatological studies weighing factors such as mean wind speed and direction. Unfortunately, the impact on nearby radar sites is often not considered and there are few regulations requiring such an investigation. In fact, the only regulation in place is the Interim Policy on Proposed

Corresponding author address: Brad Isom, School of Meteorology, University of Oklahoma, 120 David L. Boren Blvd., Suite 5900, Norman, OK 73072.
E-mail: bisom@ou.edu

DOI: 10.1175/2008JTECHA1136.1

Windmill Farm Locations issued by the Department of Defense and the Department of Homeland Security (American Wind Energy Association 2006).

Current wind farms can be collections of 100 or more individual wind turbines exceeding heights of 150 m at the blade tip and taller structures are expected in the future. Blades themselves can exceed lengths of 40 m, creating an 80-m-diameter circle of influence (American Wind Energy Association 2007b). To put this in perspective, it is useful to compare these values with a typical radar resolution gate or cell. For instance, a Weather Surveillance Radar-1988 Doppler (WSR-88D) located 30 km from a wind farm and pointing at 0.5° elevation will have a beam centered approximately 300 m above the ground with a cross-range width of about 500 m and a range depth of 250 m (Office of the Federal Coordinator for Meteorological Services and Supporting Research 2006; Doviak and Zrnić 1993). Thus, the base of the beam will be roughly 50 m above the ground at 30 km. It becomes clear that turbines occupy space that is also observed by radar systems (American Wind Energy Association 2007a,b).

So, with all of the benefits of wind-driven energy production, it becomes apparent that objects sharing the same space as the wind turbines will experience some drawbacks as well. Large wind farms have been known to provide a hazard to both migrating bird populations and bats (Department of Energy 2007b). Another unforeseen drawback to wind-generated power is interference induced on nearby radars known as wind turbine clutter (WTC). Countries, such as the United Kingdom, have initiated studies of the impact of WTC on air traffic control (ATC) radars (Poupart 2003; Spaven Consulting 2001; Webster 2005). Other studies focus on the mitigation of WTC on ATC radars and make several recommendations including increasing range resolution and employing constant false alarm rate (CFAR) algorithms, for example, Butler and Johnson (2003) and Perry and Biss (2007). Though these reports produce some promising results, no satisfactory solution to the WTC problem has been presented and the application to weather radars has not been addressed. However, an effort has been initiated within the United States to document, characterize, and mitigate the effects of WTC, specifically, for weather radars (Vogt et al. 2007).

While the characterization and mitigation methods discussed in this paper can apply to all weather radar applications, the WSR-88D system is the focus of this study. WTC is composed of two identifiable sources: the tower and the blades. The tower structure is expected to be the dominate source of interference (due to both its size and radar cross section), but can be significantly attenuated with conventional clutter-filtering techniques, which are based on the assumption of stationary targets. Wind turbine blades have a much smaller radar cross section when compared to the tower; however, removing the effects of the blade motion is much more problematic. The Nyquist velocity for weather radar varies depending on the pulse repetition frequency (PRF) with a typical maximum of 32.6 m s^{-1} (wavelength of 10 cm) (Office of the Federal Coordinator for Meteorological Services and Supporting Research 2006). Wind turbine blades with lengths in excess of 40 m can have tip velocities reaching 70 m s^{-1} (at 17 rpm) and, depending on the orientation of the rotation plane with respect to the radar beam, aliasing often occurs. Moreover, the blade face orientation changes with the wind direction directly affecting the radial component of the tip speed. The resulting Doppler spectrum can mask weather signals present in the clutter region or can falsely appear as weather signals where there are none. Two examples of 0.5° elevation reflectivity fields of WTC seen near Dodge City, Kansas, via the WSR-88D KDDC radar are shown in Fig. 1 for cases of clear air and isolated storms. Both cases were collected under normal operating conditions and have been preprocessed with the standard clutter-removal algorithm. The WTC mixed with isolated thunderstorms is shown in the right panel of Fig. 1 while clear-air WTC is shown in the left panel with the wind farm circled in black. Note that it is difficult to distinguish between the isolated storm cells and the WTC in the mixed case, even after the application of the standard clutter filter. In addition to the visual disturbance produced by WTC, the false reflectivity measurement generated from the WTC will bias the downstream products derived from the contaminated data. For example, the quantitative precipitation estimates (QPEs) would be significantly biased for the area contaminated by WTC for both cases in Fig. 1.

A description of the raw time series data collection experiments performed on two WSR-88D radars and the details of the WTC observations are given in section 2. Several mitigation techniques and a statistical examination of the methods are presented in section 3. Recommendations and possible future work are discussed in section 4.

2. Wind turbine clutter observations

a. Data collection and experiment design

Two WSR-88D sites known to experience WTC are Dodge City, Kansas (KDDC), and Great Falls, Montana (KTFX), and were chosen as the locations for two intensive experimental campaigns. The wind farm near KDDC comprises 170 individual turbines located approximately

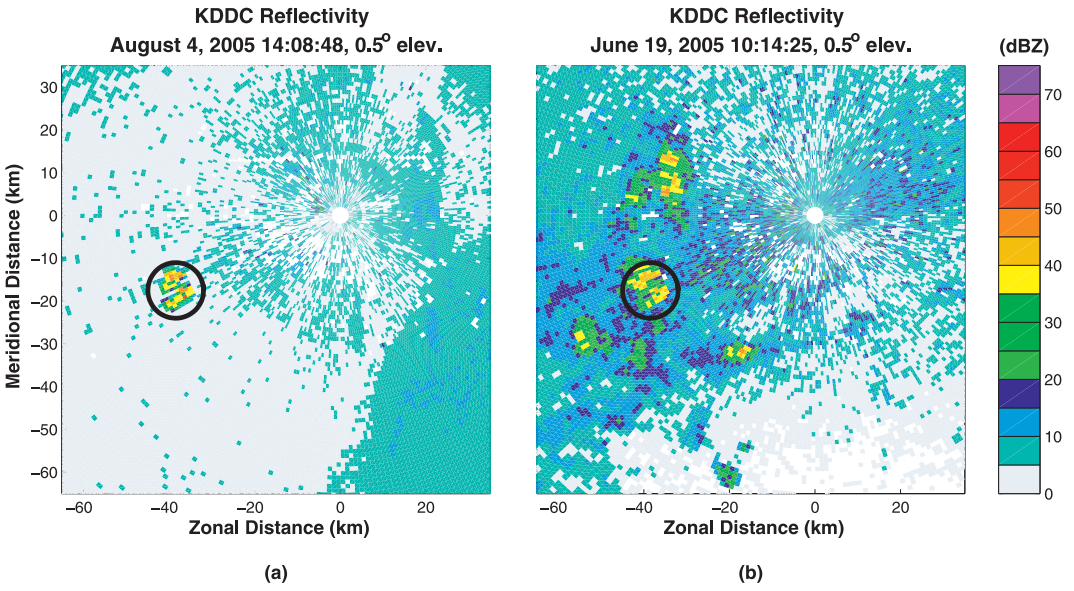

FIG. 1. An example of WTC moment data as seen from the KDDC WSR-88D. (a) The reflectivity of the wind farm is similar to (b) the reflectivity of isolated precipitation surrounding the wind farm (circled in black). This bias in reflectivity permeates to higher-level products such as precipitation estimation.

40 km southwest of the radar while the wind farm near KTFX includes 6 turbines located 6 km northwest of the radar. The goal of the experiments was to collect unfiltered time series data in a variety of formats for processing and further examination.

The experiment at Dodge City was performed on a WSR-88D with a Sigmet RVP8 digital receiver. Time series data were collected in spotlight mode (continuous data collection with a stationary antenna), range–height indicator (RHI) scan mode, and normal volume coverage pattern (VCP) scanning modes. Spotlight mode data collection was performed to examine the detailed temporal evolution of the WTC Doppler spectrum. RHI scan mode was implemented to ascertain the extent to which the WTC is detected by the antenna sidelobes. VCP scans were performed to provide cases with which to test the mitigation algorithms that were to be developed for operational usage. The highest PRF was used for the spotlight and RHI collections to maximize the Nyquist velocity and reduce the aliasing effect on the WTC Doppler spectrum. A PRF of 1282 Hz was used, resulting in a Nyquist velocity of 33.1733 m s^{-1} (wavelength of 10.35 cm). Range oversampling was implemented to obtain 25-m range gate spacing and increase the likelihood of gathering single-turbine spectra. Having multiple turbines present complicates the analysis and is discussed further in the next section. The scanning modes were left to the discretion of the operator, but several hours of data were collected using VCP 21. This VCP is generally used in convective situations and the operator has the option to adjust the PRF for the Doppler cuts (Office of the Federal Coordinator for Meteorological Services and Supporting Research 2006). In this case, the operator chose the highest PRF available.

The experiment in Great Falls was also performed with a WSR-88D using a Sigmet RVP8 digital receiver. Due to the proximity of the radar to the turbines, in addition to documenting normal WTC patterns, it was expected that observations of WTC multipath scattering effects could be obtained. The same scanning strategies used for KDDC were also used to obtain the time series data for this experiment. Data were collected in spotlight and RHI mode using a PRF of 1310 Hz (33.8983 m s^{-1} aliasing velocity) and 25-m gate spacing. Again, several hours of VCP 21 scanning data were collected.

b. *Experimental results and interpretation*

Examples of the evolution of a WTC Doppler spectrum obtained in spotlight mode for a 4-s time period for each radar site are shown in Fig. 2. To calculate the spectra 64 samples were used and a Blackman–Harris window has been applied. Careful consideration was given to the spotlight scan azimuth selection to ensure that the spectra were produced by a single turbine. While clutter signals from multiple turbines are also useful for documentation, it is beneficial to observe the effects of a single turbine for better understanding. The impacts of multiple turbines within a single gate can be observed as a repeated single-turbine pattern, shifted in time. A strong return [>60 dB signal-to-noise ratio (SNR)]

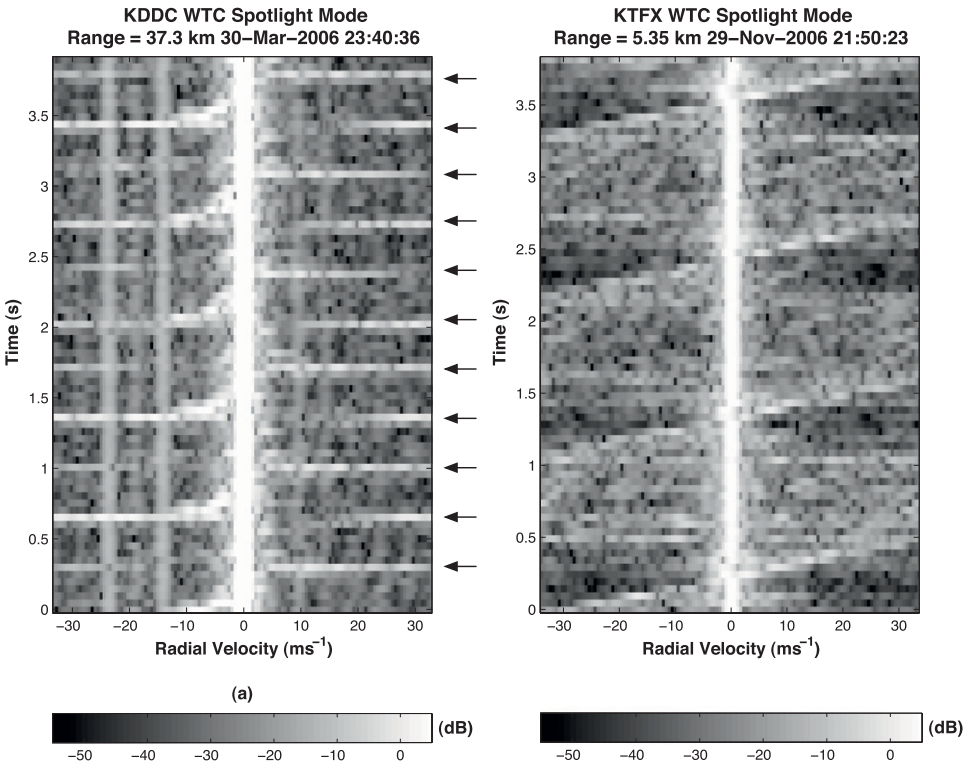

FIG. 2. Examples of the temporal evolution of the WTC Doppler spectrum for (a) KDDC and (b) KTFX at 0.5° elevation. The wind turbine tower is clearly visible at the zero Doppler velocity, while the blades are visible as periodic *flashes* spread across the spectrum, indicated by the arrows in (a). The proximity of KTFX to the turbines allows for higher returns from additional portions of the blade, thus creating a more detailed spectral image of WTC and limiting the visibility of the flashes that appear in (a).

is present at the zero Doppler velocity throughout the duration of the scan and is attributed to the wind turbine tower as it is a stationary structure. The aliased periodic rise in power level as the spectrum evolves is attributed to the echo returns from the wind turbine blades as they pass a vertical position (either straight up or down). For a three-blade wind turbine, such as the type near KDDC and KTFX, this would occur 6 times per rotation. The 23.5-m wind turbine blades for the wind farm near KDDC rotate at a fixed rate of 28.5 rpm. With this rotation rate and given the duration of the data, the turbine should have rotated approximately twice over the 3.88-s time sample. The hypothesis holds as there are 11 *flashes* visible in Fig. 2a, denoted by the arrows. In addition, it is known that the wind direction during the time of the scan was west-northwesterly at 300° and the maximum tip velocity for this particular turbine is 70 m s^{-1}. The blade face would be 41° off radial, thus making the radial component of the maximum tip velocity approximately 53 m s^{-1}. Aliased flashes in Fig. 2a confirm this calculation. The wind turbines near KTFX have a variable rotation rate that is determined by the wind speed, thus making it difficult for a similar analysis to be conducted. However, the wind direction is known and thus the blade face orientation could be calculated. While the radial component of the maximum tip speed is not known, the Doppler spectra did exhibit distinct periodic behavior due to the limited number of turbines that make up the wind farm. As such, an estimate can be calculated from the turbine blade length, 38.5 m, and examining the number of rotations visible in Fig. 2b. One rotation occurs over 3.32 s, producing a rotation rate of approximately 18 rpm and a maximum tip velocity of 73 m s^{-1}. Notice that the periodic signal recorded at KTFX, instead of the well-defined flashes from KDDC, appears as a detailed sinusoid. One possible reason for this is due to high radar sensitivity at this proximity, which may allow for the detection of additional portions of the blade that might not appear at greater distances. In addition, the turbine blade rotation rate is much slower than the turbines near KDDC and the radar is able to capture smaller portions of the blade rotation in each time frame.

Examples of spectra evolution for elevation angles between 0.5° and 2.9° obtained from the RHI scans are

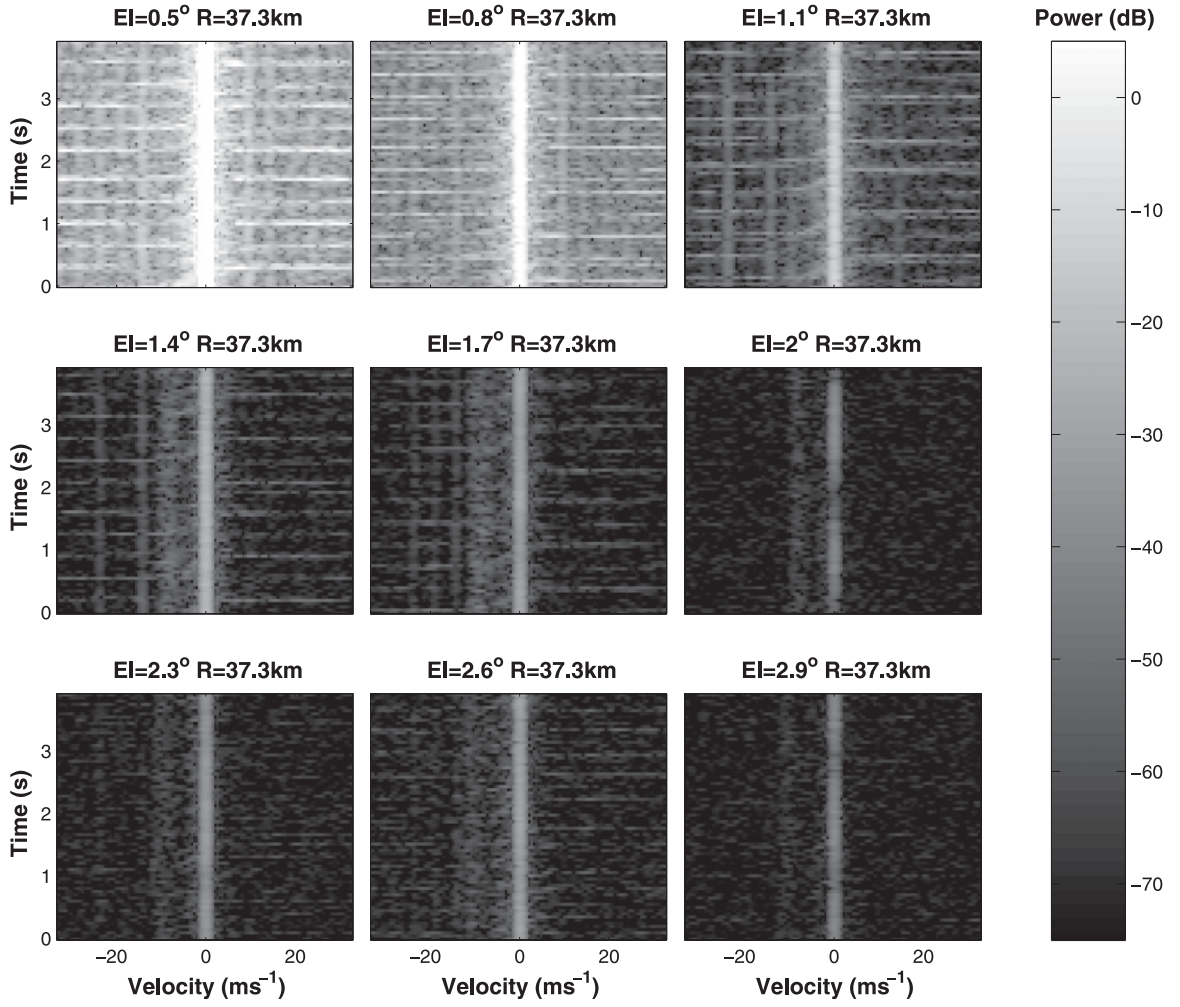

FIG. 3. RHI scan data from the 30 Mar 2006 KDDC experiment. Each elevation image was obtained by gathering data in spotlight mode to ensure blade detection. The effects of the turbine blades are minimal above 1.1°, above which the only significant contribution is from the turbine tower, which can be mitigated with conventional clutter filters. Note that the power reaches a secondary maximum at 2.6°, which is the first sidelobe angle (Sirmans 1993).

shown in Fig. 3. The first null and sidelobe of the WSR-88D antenna are at 2.1° and 2.6°, respectively (Sirmans 1993). As the elevation angle approaches 2.1°, the impact of the blades and the tower on the Doppler spectrum is reduced. Then, as the beam approaches 2.6°, the power level increases as expected. Thus, the WSR-88D antenna sidelobes will detect both aspects of WTC contamination (tower and blades) and cannot be completely ignored. In some instances, however, it is possible that the power of the weather signals would significantly exceed that of the blade signal. A significant contribution from the tower would still remain due to its radar cross section as compared to the blades and, for such cases, the remaining tower contamination could be handled by standard clutter-filtering methods to reduce the majority of the WTC effects.

As predicted, the proximity of KTFX to the wind farm allows for the measurement of WTC multipath scattering effects. These effects will cause a region of elevated power in range gates behind the wind farm. An image illustrating this effect is shown in Fig. 4. The wind farm is visible at approximately 6 km from the radar at 315° azimuth and is circled in black. The false-echo region of higher power that extends behind the wind farm is likely due to multipath scattering effects and is circled in red. It is possible that a pulse transmitted by a radar could be reflected between multiple turbines, or between a turbine and other ground targets, and could eventually settle on a trajectory leading back to the radar. Only a small percentage of the transmitted power is reflected at each stage, so the proximity to the radar is an important factor in observing this effect.

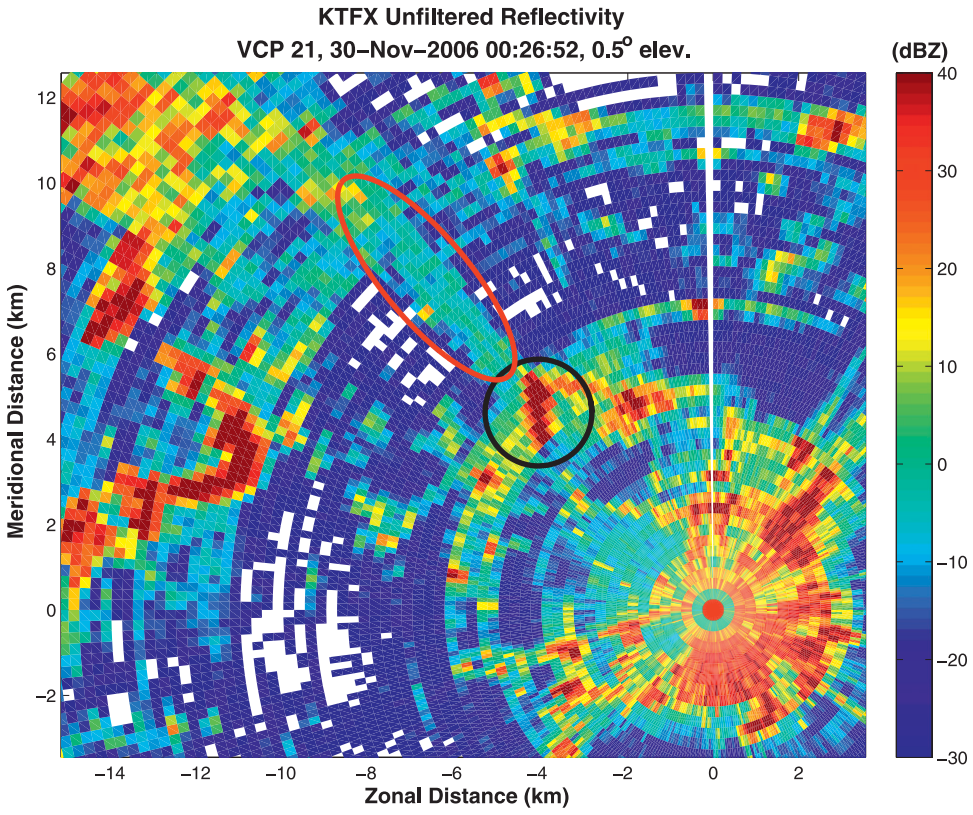

FIG. 4. An unfiltered reflectivity PPI plot of multipath scattering effects taken from KTFX. The false-echo region (circled in red) behind the wind farm (circled in black) is thought to be the result of multipath scatter between turbines, the ground, and/or the radar dish itself. The proximity of the wind farm to the radar has a profound influence on the radar sensitivity and is considered to be the main contributor to detecting this effect.

In further exploration of multipath scattering, the spectra of gates down range from the known turbine locations were examined with the expectation that the typical WTC Doppler spectra would be present but at a much lower power. As seen in Fig. 5, this is indeed the case. Typical WTC Doppler signatures can be identified at distances surpassing 13 km despite the significant decrease in power.

3. Wind turbine clutter mitigation

Several conventional clutter-filtering techniques, such as finite impulse response (FIR) filters and Gaussian model adaptive processing (GMAP) (Doviak and Zrnić 1993; Siggia and Passarelli 2005), have been implemented and have not produced favorable results with respect to wind turbine clutter suppression, as expected. The turbine and weather spectra can occupy the same Doppler frequency span and share a similar dynamic range, causing conventional methods to fail in isolating the weather signal. The solution that has yielded satisfactory results and will be discussed hereafter makes use of multiquadric interpolation and attempts to mask the impact of the WTC. As with any interpolation scheme, resolution is lost during the processing.

a. Creation of a dataset for objective examination

The data collected during the experiments described in section 2 do not contain any mixed weather and WTC signals. Data collection was not possible during times where severe weather was a possibility since spotlight and RHI scans require the operator to relinquish control of the radar. To test the effectiveness of the mitigation algorithm on cases other than clear air, a test set of data was created by combining separate weather signals with WTC through a simple direct sum of the time series of the in-phase and quadrature (I–Q) voltage values. This could be achieved by the fact that the data were recorded in time series format. Conventional processing techniques could still be used to calculate the three spectral moments of interest: reflectivity, radial velocity, and spectrum width (Doviak and Zrnić 1993). Only scans with similar PRFs

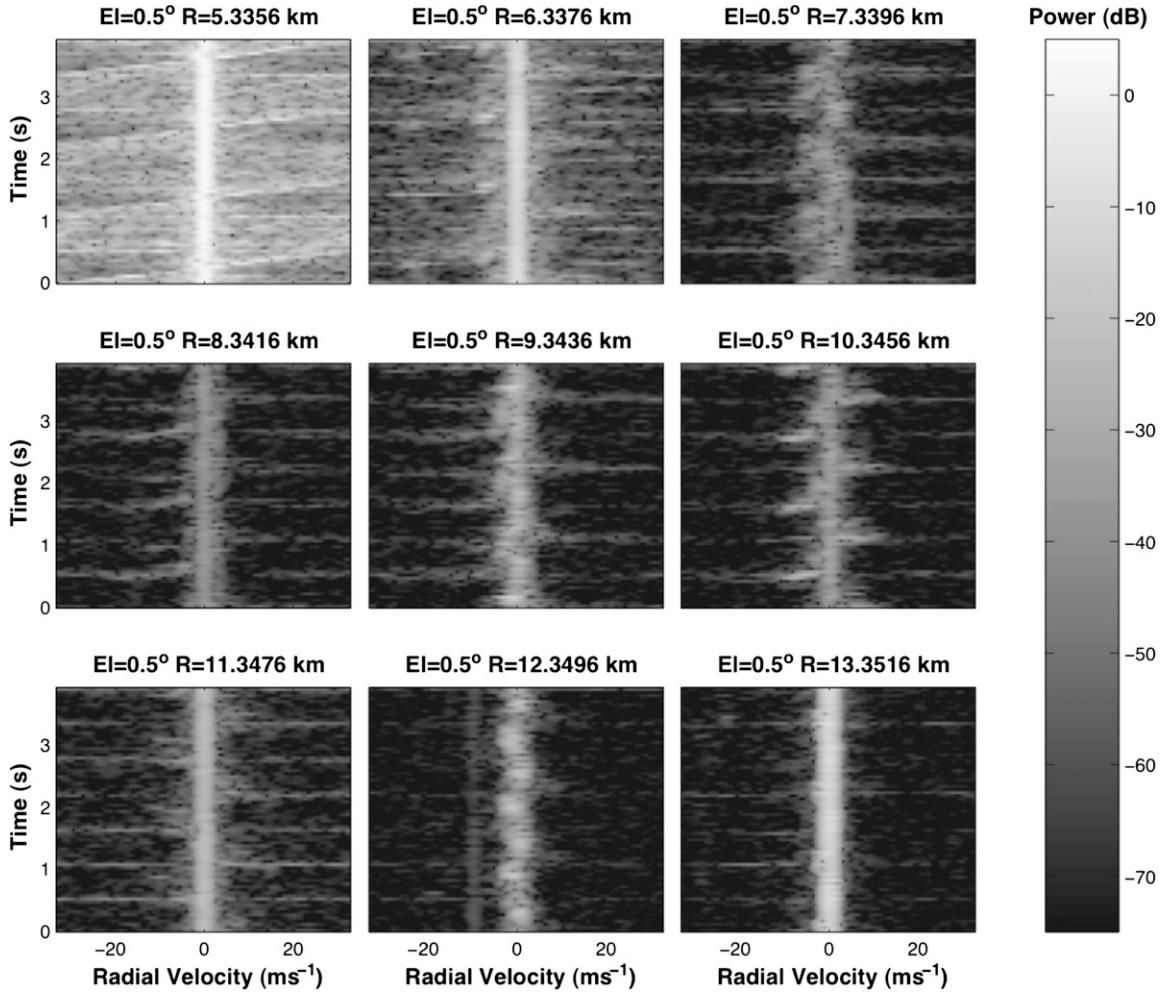

FIG. 5. The evolution of the Doppler spectra over increasing range gates along the 315° radar radial for KTFX. The wind turbine is present at approximately 5.3 km and is identified by the typical Doppler patterns associated with WTC in spotlight mode. Similar patterns are present down range of the known turbine location and indicate the presence of energy that at one point made contact with a rotating turbine blade.

were combined to ensure minimal artifacts that might result from the dataset creation. Also, precisely the same range gates were used from each scan to preserve sampling volumes. Using this scheme, any interaction between the weather and wind turbine echoes is absent but such effects are thought to be insignificant. The separate and combined signals allowed for objective measurements to be made regarding the efficiency of the mitigation algorithm without the use of synthetic data.

b. Multiquadric interpolation and spatial data

Multiquadric interpolation was first proposed by Hardy (1971) as a means of creating a regularly spaced grid from irregularly spaced topographical data. Franke (1982) explores several global interpolation techniques and ranks the multiquadric method among the highest. Nuss and Titley (1994) make use of multiquadric interpolation with meteorological data and find it outperforms both the Cressman and Barnes techniques, although the extent of their claims of better performance versus the Barnes method were later challenged by Barnes (1995). While Nuss and Titley (1994) perform their comparison on smooth fields such as temperature and pressure, the original intent of Hardy (1971) was for multiquadric interpolation to be used on highly variable topographic data, a natural spatial phenomenon. With the exception of velocity aliasing, it is believed that the multiquadric method is applicable to the highly variable products of weather radar. Multiquadric interpolation is a global interpolation technique that uses radial basis functions to approximate missing data, reflectivity in this case, through the following equation:

$$Z(X) = \sum_{i=1}^{N} \alpha_i Q(X - X_i), \quad (1)$$

and $Q(X - X_i)$ is a radial basis function defined as

$$Q(X - X_i) = (\|X - X_i\|^2 + b^2)^{1/2}, \quad (2)$$

where $X - X_i$ is the distance from any point X_i to a central point X and b is a user-defined constant (typically around 0.391 for this case). Rippa (1999) discusses several methods for selecting the constant b. Much care must be given to the selection of this parameter as large values of b can lead to system instability. The α_is are found by simply solving the set of linear Eqs. (1) resulting from a group of N known observations. The unknown value is then determined using the calculated weights. While reflectivity is used in Eq. (1), any spatially varying field can be interpolated (Nuss and Titley 1994) provided that a new set of α_is is generated for each.

c. *Interpolation schemes and nowcasting*

One of the most important tasks prior to the application of any interpolation scheme is simply identifying which data points to use. In this application of multiquadric interpolation, field values of gates corrupted with WTC are to be replaced with data fitted to a surface comprising uncontaminated field values. Both contaminated and uncontaminated data points are established a priori and stored in a static file. WTC-corrupted points were identified by examining several clear-air scans and applying a simple thresholding technique. Latitudes and longitudes of individual turbines were also used to verify the identification scheme. An interpolation window extends from the borders of the corrupt region with a range approximately matching the width–depth of said region. Studies examining the necessary interpolation window size for WTC scenarios are incomplete at this time; however, larger windows may stray from the assumption of spatial continuity necessary for global interpolation schemes.

The aforementioned multiquadric interpolation can be applied to the spectral moments in both two and three dimensions. The third dimension is included by utilizing the higher-elevation cuts from the same VCP scan that do not contain interference from the WTC. Additionally, the multiquadric method can be used to interpolate each spectral component by treating each spectral bin as a separate data field and will herein be referred to as spectral interpolation. It is expected that the spectral interpolation will preserve the fine features of the Doppler spectrum and increase the accuracy of the estimated moments. The three-dimensional interpolation is also expected to provide a more accurate representation of the storm structure and again increase the accuracy of the algorithm provided the storm occupies multiple elevations.

Nowcasting is a short-term forecast that attempts to incorporate the temporal continuity of weather into traditional forecasting and is explored here as an enhancement to the effectiveness of the interpolation algorithms discussed before. Many techniques exist that identify storm cells or particular features of storms and track the motion over several temporal frames. The Storm Cell Identification and Tracking (SCIT; Johnson et al. 1998) algorithm and the Machine Intelligent Gust Front Algorithm (MIGFA; Delanoy and Troxel 1993) are two such techniques and are extremely effective in their designed tasks, but are overly complicated for the WTC scenario, at least at this early stage of development. For WTC mitigation, temporal evolution is incorporated by employing a simple nowcasting technique that was adapted from an early method developed by Rinehart and Garvey (1978). A two-dimensional cross correlation is calculated between a designated sector of the current and previous PPI reflectivity images. Due to the inherent difficulties of advecting a three-dimensional field, when only one dimension (radial) is sampled, radial velocity was not considered. The sizes of the sectors were determined by estimated maximum storm velocities and the revisit times of the WSR-88D (Office of the Federal Coordinator for Meteorological Services and Supporting Research 2006). The first moment is calculated for the two-dimensional cross correlation giving the spatial shift between the PPI images. The previous scan data are then translated in the determined direction. The next step is to combine the translated and interpolated data in an optimum way, which is accomplished via a least mean squares scheme. First, a set of test gates are selected outside of the contaminated region where the interpolated, nowcasted, and true values are all either calculated or known. Next, a least mean squares criterion is used to calculate weights that minimize the mean square error between the linear combination of the interpolated and nowcasted values and the true values. Finally, the weights are used in the contaminated region to optimally combine the interpolation and nowcasting data and will herein be referred to as the hybrid technique. This procedure is summarized below for clarity and the optimization process is further described in mathematical terms.

1) Calculate the two-dimensional cross correlation over a specified window with current and previous scans as input;
2) calculate the first moment of the cross correlation to reveal the motion vector;

TABLE 1. RMS errors for the KDDC WTC and an isolated cell event.

	Isolated cell							
	2028:31 UTC		2034:17 UTC		2040:04 UTC		2045:50 UTC	
Algorithm	$RMS_{\hat{Z}}$ (dBZ)	$RMS_{\hat{v}_r}$ (m s^{-1})	$RMS_{\hat{Z}}$ (dBZ)	$RMS_{\hat{v}_r}$ (m s^{-1})	$RMS_{\hat{Z}}$ (dBZ)	$RMS_{\hat{v}_r}$ (m s^{-1})	$RMS_{\hat{Z}}$ (dBZ)	$RMS_{\hat{v}_r}$ (m s^{-1})
WTC	27.6070	12.8613	13.4982	8.7934	15.2195	16.8399	31.6210	11.1529
2D moment	8.1303	11.3302	5.7855	1.4576	5.5623	1.4877	11.9729	10.6476
2D spectral	10.6675	11.0434	6.9375	2.2341	6.7634	2.2790	14.8298	10.0740
3D moment	7.0959	9.0445	6.5328	1.4117	5.4530	1.1755	9.0877	10.4177
3D spectral	6.1377	7.3831	5.8819	1.2767	6.1403	0.9995	7.8769	10.1200
2D hybrid	6.9237	—	5.4458	—	5.1488	—	8.8539	—
1D linear	7.5231	7.9727	8.4629	2.6438	9.6937	1.9190	11.1049	11.3210

3) translate the previous scan according to the motion vector;
4) compute the optimized weights by completing a least squares analysis on the translated, interpolated, and known values for a set of test gates; and
5) combine the interpolated and advected data using the optimized weights.

The following equation describes how the interpolated power estimates (P_{i1}, . . . ,P_{ik}) are combined with the nowcasting power estimates (P_{n1}, . . . ,P_{nk}) to form a single estimate vector $\mathbf{P}_c$:

$$\mathbf{P}_c = \mathbf{w}^{\mathrm{T}} \begin{pmatrix} P_{i1} & P_{i2} & \cdots & P_{ik} \\ P_{n1} & P_{n2} & \cdots & P_{nk} \end{pmatrix} = \mathbf{w}^{\mathrm{T}}\mathbf{P}, \tag{3}$$

where $\mathbf{w}$ is the $[2 \times 1]$ weighting vector determined by minimizing the cost function,

$$J = E[(\mathbf{P}_t - \mathbf{P}_c)^2], \tag{4}$$

and $\mathbf{P}_t$ is the test-gate vector with $E[\cdot]$ representing the expected value. The minimization of J with respect to $\mathbf{w}$ results in the following solution:

$$\mathbf{w} = (\mathbf{P}\mathbf{P}^{\mathrm{T}})^{-1}\mathbf{P}\mathbf{P}_t^{\mathrm{T}}. \tag{5}$$

The selection of the test area, represented by $\mathbf{P}_t$, is a step of considerable importance for the nowcasting–interpolation hybrid algorithm. The test area cannot be located behind the wind farm as multiturbine scattering effects may contaminate the data. Also, if the weather event is moving across the WTC region toward the chosen test area, it is likely that contaminated cells will translate into the test region reducing the number of test gates and therefore diminishing the usefulness of the entire testing procedure. To avoid this problem, a narrow (≈1 km) band of test cells is chosen, encompassing the three remaining sides of the farm.

d. Interpolation testing and results

Time series data for two weather events were used to test the interpolation algorithms on the KDDC WTC case. The first was an isolated cell recorded by KDDC on 30 March 2006 and the second was a squall line recorded by KTLX near Oklahoma City, Oklahoma, on 24 April 2007. The data were combined with KDDC WTC data collected on 30 March 2006 in the manner described earlier. Six interpolation schemes were used on each weather case over four scans of equal temporal distance. The four scans provide a variety of weather–WTC scenarios that include the weather event entering, overlapping, and exiting the WTC region. There are many techniques that can be used to quantify the quality of an image with respect to an original that take the human visual system (HVS) into consideration (Eskicioglu and Fisher 1995). However, for the sake of simplicity, a root-mean-square (RMS) error evaluation is used for this study. The values presented in Tables 1 and Tables 2 were obtained by calculating the RMS errors between the original and corrected reflectivity ($\hat{Z}$) and radial velocity ($\hat{v}_r$) PPI images for each weather case and interpolation technique. Only the interpolated region was considered in the RMS error analysis and a 5-dB SNR was required for the gate to be included in the interpolation or error analysis.

For the purpose of comparison, a one-dimensional linear regression fit was performed along the radials for each case study and the results are given in Tables 1 and Tables 2. In some instances, the linear regression technique outperforms the multiquadric method. For example, it appears that for scenarios in which the weather has passed or is overlapping the wind farm, the regression technique performs better, especially for the radial velocity fields, but only for the two-dimensional cases and one three-dimensional moment case. Linear regression does not outperform either the three-dimensional spectral or hybrid technique for any scenario. It is believed that multiquadric interpolation is more sensitive

TABLE 2. RMS errors for the KDDC WTC and KTLX squall-line events.

	Squall line							
	1836:26 UTC		1846:16 UTC		1856:07 UTC		1905:57 UTC	
Algorithm	$RMS_{\hat{Z}}$ (dBZ)	$RMS_{\hat{v}_r}$ (m s^{-1})	$RMS_{\hat{Z}}$ (dBZ)	$RMS_{\hat{v}_r}$ (m s^{-1})	$RMS_{\hat{Z}}$ (dBZ)	$RMS_{\hat{v}_r}$ (m s^{-1})	$RMS_{\hat{Z}}$ (dBZ)	$RMS_{\hat{v}_r}$ (m s^{-1})
WTC	12.2603	10.8399	1.2773	7.1849	3.8860	4.3457	22.6609	9.1110
2D moment	4.2619	4.2712	4.5854	1.5187	4.6675	1.3723	6.2629	4.2489
2D spectral	4.7785	2.1246	5.3670	1.7384	5.6841	1.4217	7.5219	4.7150
3D moment	4.2945	1.9859	3.7226	1.3217	4.4612	1.1575	4.5461	2.4483
3D spectral	5.1328	1.7137	5.2128	1.4588	4.6469	1.2380	4.3925	1.8818
2D hybrid	4.2731	—	4.4911	—	4.9157	—	6.2738	—
1D linear	9.4155	2.8871	10.8524	4.1902	7.6274	1.5523	8.0464	1.9345

to the noise introduced by weak weather signals than linear regression and may account for this effect. While multiquadric interpolation is the primary technique examined here, it is shown by the linear regression comparison that other interpolation algorithms may prove more appropriate for particular fields, weather scenarios, or wind farms. However, in many cases, multiquadric interpolation provides more accurate corrections.

The application of the interpolation algorithms to the isolated cell case largely improved the reflectivity and radial velocity estimations as summarized in Table 1. However, assumptions that the spectral interpolation would significantly improve the radial velocity estimations do not hold. For most cases, the improvement does not justify the increase in computational complexity incurred by performing the interpolation on each spectral component. In fact, the two-dimensional spectral interpolation performs worse than the two-dimensional moment interpolation for scans at 2034:17 and 2040:04 UTC. Noisy data present in the PPI scan can cause inaccuracies in the interpolation output. In particular, gates near the border of the interpolation region pose a problem due to the fact that the weights determined by the multiquadric method are a function of distance as well as magnitude. The likelihood for corruption due to noise is greater for the spectral interpolation method since any signal present in a discrete frequency is considered for the interpolation, as compared to the moment interpolation where only a single value is considered for each gate. One solution to this problem is to expand the WTC exclusion zone to include gates that do not contain wind turbines but are affected by infrequent interference. Another possible solution involves smoothing the data prior to the interpolation, thus suppressing potential noise corruption (Nuss and Titley 1994). In contrast, the assumption that the three-dimensional interpolation would outperform the two-dimensional interpolation holds true for the isolated cell case. The inclusion of the higher elevations in the interpolation scheme enhances the accuracy of the algorithm. Finally, the nowcasting–interpolation hybrid algorithm outperformed the two-dimensional moment interpolation in each case presented in Table 1.

The squall-line case exhibits much of the same results as those of the isolated cell case and the results are shown in Table 2. The spectral interpolation does not provide an appreciable gain in velocity estimations but the three-dimensional interpolation does improve the estimates over the two-dimensional schemes. This is true for all but the 1836:26 UTC scan where the three-dimensional schemes actually perform worse than the two-dimensional schemes for reflectivity estimations. This may be due to the high gradient in the reflectivity values within the interpolation window or the higher elevations included in the algorithm may not accurately represent the 0.5° cut. Though the three-dimensional schemes do not perform as well as the two-dimensional schemes for this particular scan, it is important to note the improvement over the original corrupted image. The high weather reflectivity values for the squall-line case in the 1846:16 and 1856:07 UTC scans mask the interference caused by the blades, and the interpolation schemes actually increase the reflectivity estimation error by smoothing the dominate weather signal. However, for these same scans, the blade interference does bias the radial velocity estimates and the interpolation schemes provide adequate radial velocity error correction. The slow movement of the squall line did not allow many replacement gates to propagate into the WTC region. As a result, the weighted nowcasting values from the least squares combination act as a slight interference to the interpolation algorithm and increase the estimation error for the hybrid technique.

In both cases, the interpolation algorithms improve the accuracy of the reflectivity fields when the WTC bias is equal to or less than that of the weather. Strong weather reflectivity values (relative to the WTC) will mask contamination due to WTC and should therefore not be modified. Radial velocity values are much more

likely to be affected by WTC and therefore more likely to benefit from interpolation. While the multiquadric method detects the high-frequency changes present in reflectivity values, this can potentially prove counterproductive for extremely smooth fields such as radial velocity. In some instances, it may be more appropriate to consider linear interpolation as opposed to the multiquadric method for smooth fields.

While a quantitative assessment of the mitigation schemes is essential to this work, a qualitative examination is also useful. Time-lapse images of the isolated cell reflectivity and radial velocity measurements, respectively, are provided in Figs. 6 and Figs. 7. The corrupted images are shown in the left-most columns of Figs. 6 and Figs. 7 and the corrected images in the rightmost while the original weather data are displayed in the center. Listed on the right axis of each corrected image is the calculated RMS error. The storm traverses the interpolation window rapidly and exhibits weak reflectivity values. In fact, the WTC echoes are stronger than the weather in some gates. The leading and trailing edges of the isolated cell are just overlapping the WTC region in the 2028:31 and 2045:50 UTC scans, respectively, and the interpolation algorithm removes the majority of the WTC, but there are some gates with low residual reflectivity values. The overall improvement of the PPI images is notable.

The Doppler spectrum of each range gate for the 243° radial is shown in Fig. 8. The spectra have been filtered for stationary clutter and the black diamonds represent the radial velocity estimates for each gate. The wind farm occupies a continuous set of gates along the radial from 37 to 44 km. The weather signal is seen at approximately -10 m s^{-1} at the bottom and shifts slightly to -15 m s^{-1} at the top. The data were filtered for stationary clutter so the interference from the tower is removed but the blade interference remains and is visible in Fig. 8a. After the application of the interpolation algorithm, the shape of the weather signal is restored and the radial velocity estimates appear to follow a much more natural path. Some loss of resolution is visible in the time-lapse reflectivity images after the interpolation, but the quantitative and qualitative improvements are significant.

Shown in Fig. 9 are the time-lapse images of the squall-line case reflectivity again with the application of the three-dimensional spectral interpolation algorithm. The homogeneity of the radial velocity field in this case creates a qualitatively trivial exercise of the interpolation algorithm and for this reason the image is not shown. The first reflectivity scan, at 1836:26 UTC, shows the leading edge of a strong convective squall line as it arrives over the WTC region. Visually, the spectral interpolation maintains the leading boundary through the interpolated gates. The weather reflectivity values for 1846:16 and 1856:07 UTC are as high or much higher than the bias created by the turbine blades. Still, the algorithm provides a good representation of the true weather in these cases, albeit slightly smoothed.

The results of the nowcasting–interpolation hybrid method applied to the reflectivity field for the isolated cell case are presented in Fig. 10. Again, time-lapse images of the corrupted, original, and corrected data are shown in the left, center, and right columns, respectively. The rapid motion of the storm facilitates the accurate use of the nowcasting portion of the algorithm by translating many replacement or *clean* gates into the WTC region. Slower-moving weather events do not accomplish this and the interpolation portion of the algorithm is assigned a greater weight through the least squares operation. The hybrid algorithm shows improvement over the two-dimensional moment interpolation, indicating that the addition of the nowcasting holds some promise for future use. However, further refinement of the algorithm is necessary before it is ready for operational deployment.

e. Additional mitigation efforts

While the mitigation algorithms developed in this work focus on masking the contaminated weather data, other techniques are being explored that require collaborative efforts between government entities and the wind power industry. Careful consideration of wind turbine locations could enhance the effectiveness of interpolation techniques discussed here. One suggested arrangement of turbines mimics a *checkerboard* pattern with respect to the radar PPI grid. It is supposed that the number of uncontaminated gates within the wind farm would increase dramatically and thus, intuitively, so would the effectiveness of any interpolation scheme. While multipath effects, surface area requirements, and considerations for overlapping radar coverage patterns complicate the implementation of such strategies, the viability of alternative wind farm spatial patterns is being explored nevertheless.

4. Conclusions and future work

Experiments were conducted at two WSR-88D sites to gather WTC time series data. The experiments on 30 March 2006 at Dodge City, Kansas (KDDC), and 30 November 2006 at Great Falls, Montana (KTFX), provided two cases through which observations of WTC on weather radars was completed. VCP scans collected during the experiments were used in combination with two weather events to test several interpolation schemes

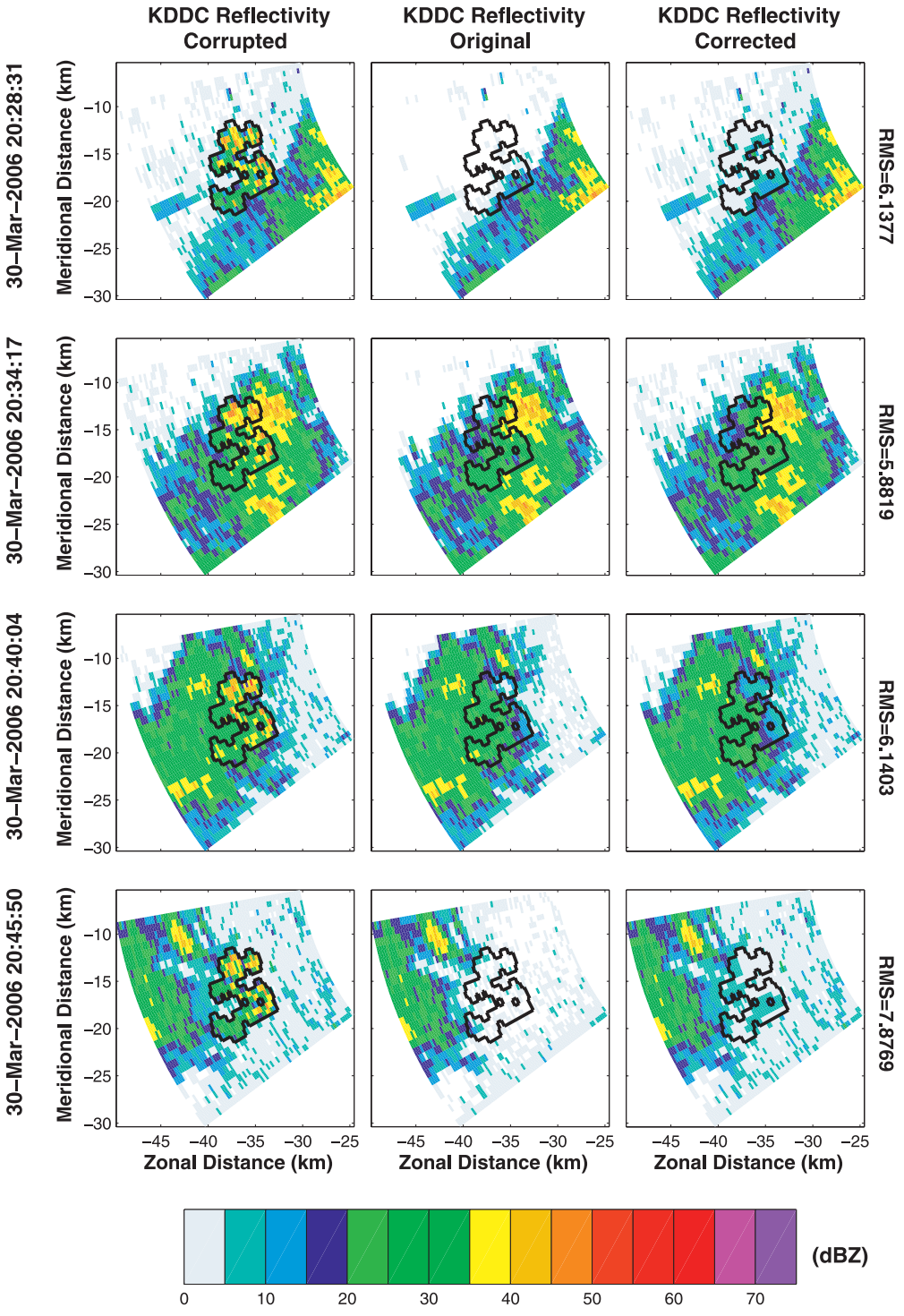

FIG. 6. A time lapse (four frames) of the three-dimensional spectral interpolation technique applied to an isolated cell event combined with WTC. Both datasets were collected at KDDC on 30 Mar 2006 at 0.5° elevation. The reflectivity was calculated from the interpolated spectra. (right) The corrected scans, (left) the WTC-contaminated weather plots, and (middle) the reference weather-only. The RMS for each example is displayed on the *y* axis of the corrected plot. Second-trip echoes are visible just down range of the wind farm and extend to the edge of the interpolation region. The interpolation scheme does not *recover* the weather data and results in a loss of resolution within the contaminated region. However, there is a substantial improvement over the contaminated image.

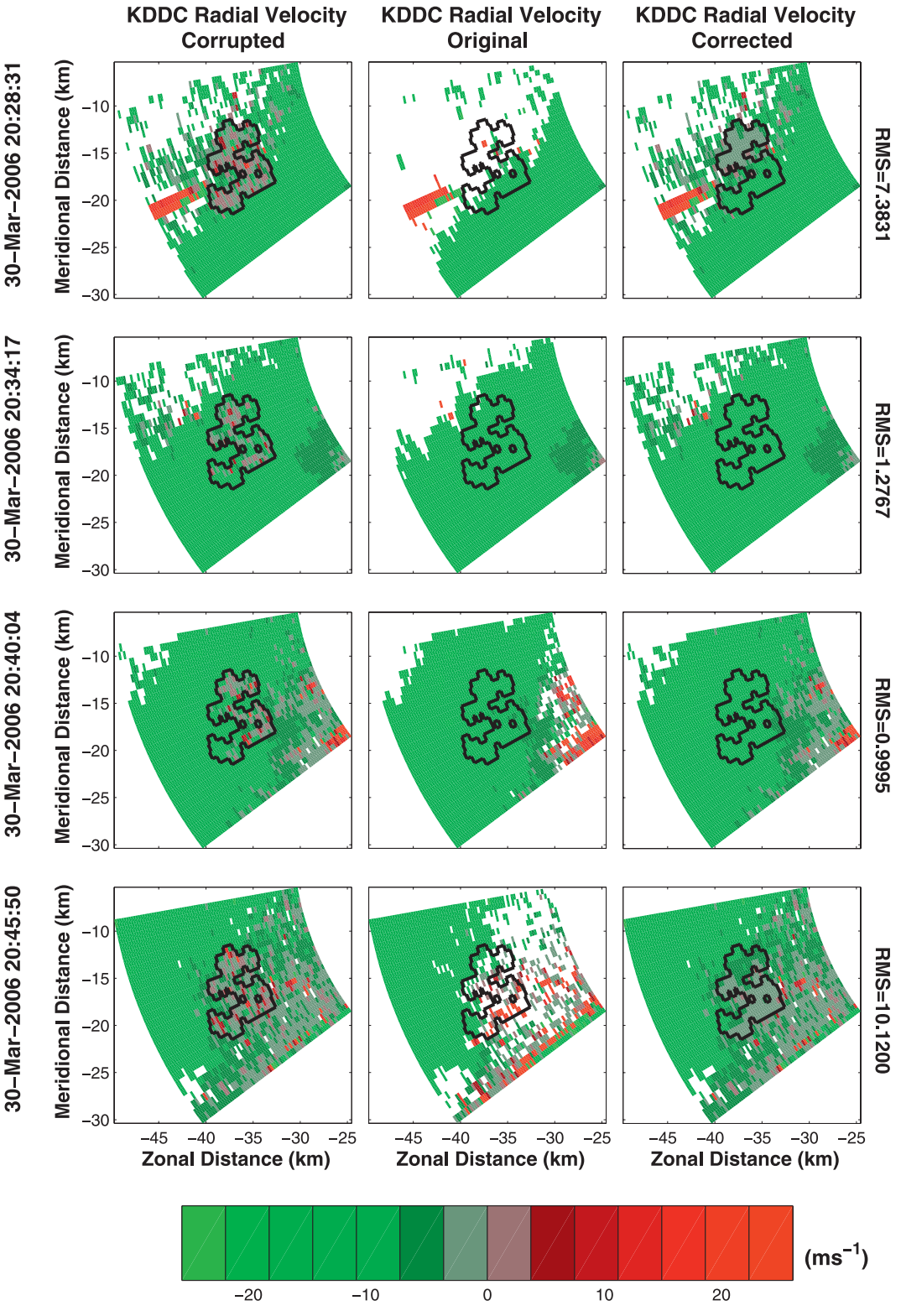

FIG. 7. As in Fig. 6, but for the radial velocity field. The loss of resolution on the radial velocity plot is not as apparent as in the reflectivity image but is still present and is reflected in the RMS error. Again, the improvement over the corrupted image is substantial.

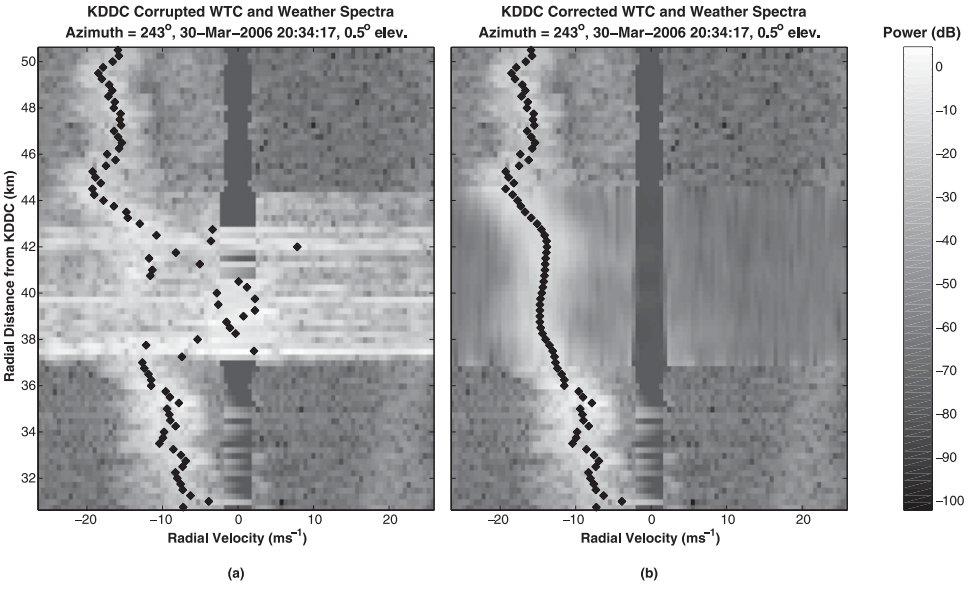

FIG. 8. WTC-contaminated weather spectra as a function of range from KDDC at a single azimuth angle (a) without the application of the three-dimensional spectral interpolation scheme and (b) with its application. Both (a) and (b) have been filtered for stationary clutter. The black diamonds represent the mean velocity at each range gate. The multiquadric spectral interpolation was applied between approximately 37 and 45 km, and the results are shown in (b).

discussed in this paper. The schemes utilize an interpolation method employing radial basis functions developed by Hardy (1971). The multiquadric interpolation algorithm was applied in two and three dimensions and to various products of time series signals and was shown to be effective in WTC masking. For comparison, a one-dimensional linear regression technique was implemented and the results show the superiority of the multiquadric method in most cases. Specifically, the three-dimensional techniques outperformed the linear regression in all but one case. While the multiquadric interpolation scheme worked well in most cases, noise present in the data, as in most interpolation schemes, has the potential to reduce the accuracy of the technique. Spectral interpolation is especially vulnerable to such noise as it is more likely that noise present in the spectra will not be carried to the moment data. In addition, velocity aliasing is a concern that has not been addressed given that the sharp velocity discontinuities of aliasing would be smoothed by any interpolation scheme. Of course, if aliasing occurred within a wind farm, the expected discontinuity would already be lost due to the random nature of the WTC velocity contamination.

Additionally, a simple nowcasting technique was used in conjunction with the interpolation scheme through a least mean squares optimal combination and the results show promise. The hybrid technique also outperformed the linear regression technique in every case. Storm velocity plays an important role in the effectiveness of the nowcasting technique. Slow-moving storms do not advect sufficient amounts of clean data into the interpolation region and thus no improvement over the interpolation schemes is noted. The interpolation schemes presented in this paper provide a method by which the impact of WTC on downstream products can be significantly reduced, though additional testing is required. Given the statistical results of this work, it can be argued that it is computationally prudent to explore the operational implementation on the base moments rather than the Doppler spectra.

Current and future research includes exploration of adaptive clutter filtering, automatic detection of contaminated cells, and polarimetric measurements. In addition, the University of Oklahoma is partnered with the National Oceanic and Atmospheric Administration's (NOAA) National Severe Storms Laboratory to explore the possible mitigation of WTC using adaptive phased-array radars. Promising results have already been obtained based on this *spatial filtering* concept and will be presented in a future publication. Finally, anechoic chamber experiments are currently under way with scaled turbine models, outfitted with sensors to measure blade rotation rate, angle, etc., to explore the possibility of adaptive filtering using data from the wind turbines themselves in real time.

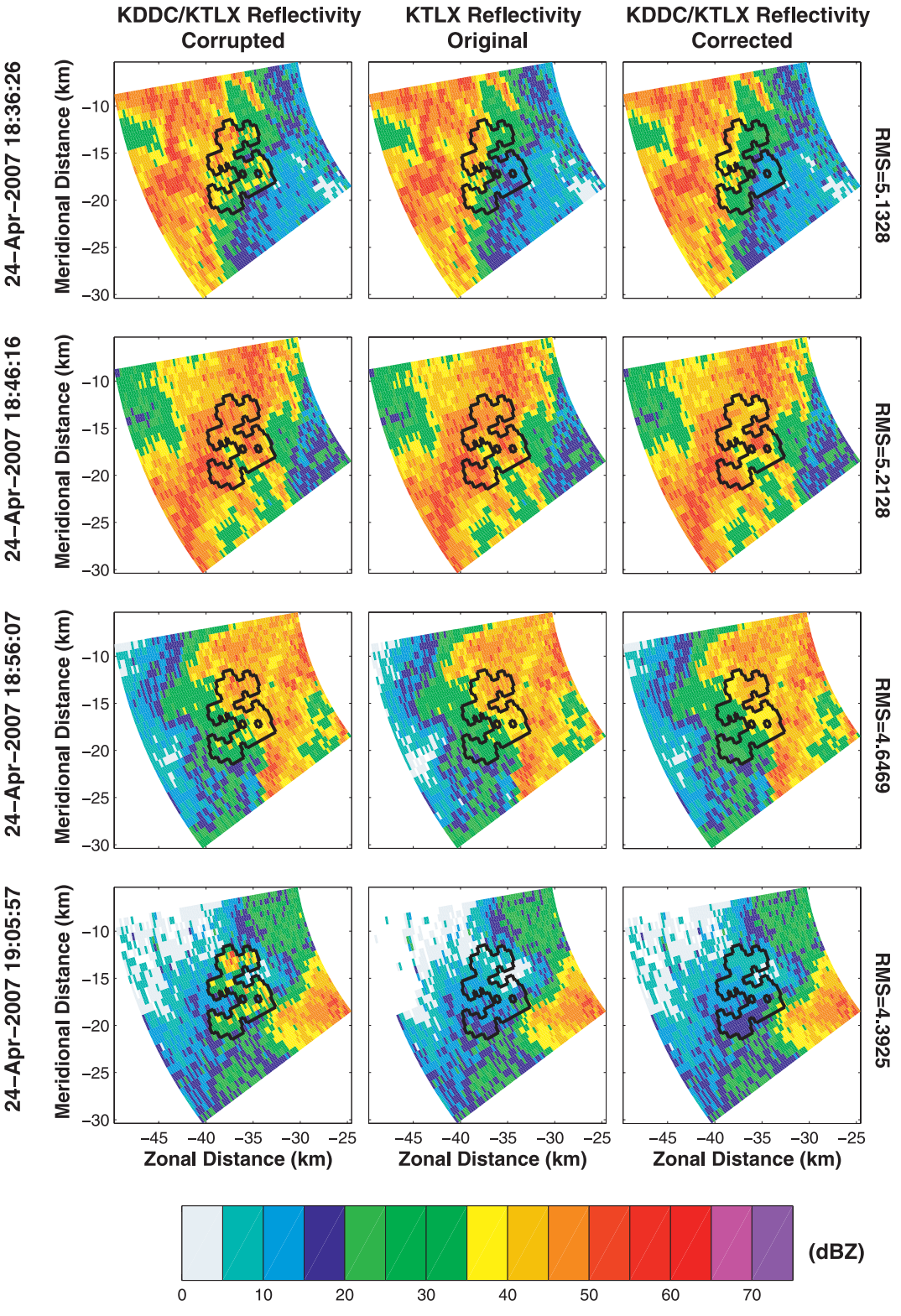

FIG. 9. As in Fig. 6, but for a squall-line event recorded at KTLX on 24 Apr 2007 at 0.5° elevation.

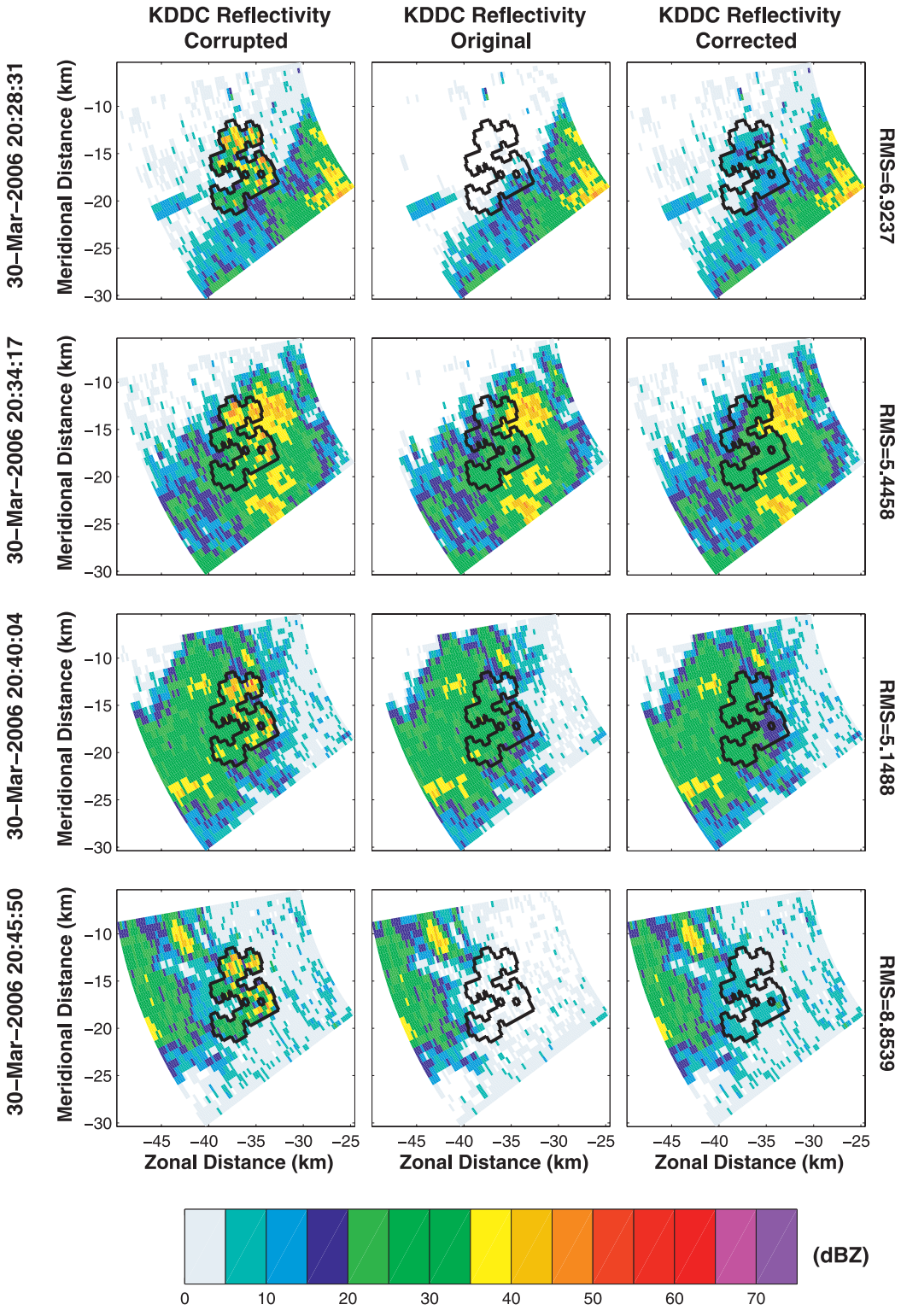

FIG. 10. As in Fig. 6, but for the two-dimensional nowcasting–interpolation hybrid scheme performed on an isolated cell event recorded at KDDC on 30 Mar 2006 at 0.5° elevation. The speed with which the storm traverses the interpolation window allows many *clean* gates to propagate into the wind farm region. These translated values are combined with the two-dimensional moment interpolation values via a least mean squares algorithm. A loss of resolution is incurred, but the overall improvement is again appreciable.

The ever-pressing need for *green* technologies will continue to drive the wind-generated power market to build increasingly larger turbines and wind farms. While site selection is carefully planned to maximize power generation, there are no current regulations to examine WTC impacts on radar sites. Cooperation between government entities and wind power companies in careful site selection could greatly improve the effectiveness of the mitigation schemes presented in this paper by increasing the number of uncontaminated gates within the WTC region. It is hoped that this work will provide a means by which environmentally conscious power production and national security interests can be simultaneously preserved.

Acknowledgments. This research was funded by the National Weather Service Radar Operations Center through Grant NA17RJ1227.

REFERENCES

American Wind Energy Association, 2006: Wind turbines and radar: An informational resource. AWEA Rep., 3 pp. [Available online at www.awea.org/pubs/factsheets/060602_Wind_Turbines_and%20_Radar_Fact_Sheet.pdf.]

——, 2007a: Wind energy–How does it work. AWEA Rep., 2 pp. [Available online at www.awea.org/pubs/factsheets/Wind_Energy_How_does_it_Work.pdf.]

——, 2007b: Wind power today. AWEA Rep., 2 pp. [Available online at www.awea.org/pubs/factsheets/WindPowerToday Final.pdf.]

Barnes, S. L., 1995: Comments on ''Use of multiquadric interpolation for meteorological objective analysis.'' *Mon. Wea. Rev.,* **123,** 2255–2256.

Butler, M. M., and D. A. Johnson, 2003: Feasibility of mitigating the effects of windfarms on primary radar. Alenia Marconi Systems Ltd. Contractor Rep. ETSU W/14/00623/REP, DTI PUB URN 03/976, prepared for British Wind Energy Association, 71 pp. [Available online at www.bwea.com.]

Delanoy, R. L., and S. W. Troxel, 1993: Automated gust front detection using knowledge-based signal processing. *Record of the 1993 IEEE National Radar Conf.,* Boston, MA, IEEE, 150–155.

Department of Energy, 2007a: Annual report on U.S. wind power installation, cost, and performance trends: 2006. Energy Efficiency and Renewable Energy Rep. DOE/GO-102007-2433, 24 pp.

——, 2007b: Renewable energy consumption and electricity preliminary 2006 statistics. Energy Information Administration Rep., 18 pp. [Available online at http://www.eia.doe.gov/cneaf/solar.renewables/page/prelim_trends/pretrends.pdf.]

——, 2007c: Wind power today. Energy Efficiency and Renewable Energy Rep. DOE/GO-102007-2424, 12 pp.

Doviak, R. J., and D. S. Zrnić, 1993: *Doppler Radar and Weather Observations*. 2nd ed. Academic Press, 562 pp.

Eskicioglu, A. M., and P. S. Fisher, 1995: Image quality measures and their performance. *IEEE Trans. Commun.,* **43,** 2959–2965.

Franke, R., 1982: Scattered data interpolation: Tests of some methods. *Math. Comput.,* **38,** 181–200.

Hardy, R. L., 1971: Multiquadric equations of topography and other irregular surfaces. *J. Geophys. Res.,* **76,** 1905–1915.

Johnson, J. T., P. L. MacKeen, A. Witt, E. D. Mitchell, G. J. Stumpf, M. D. Eilts, and K. W. Thomas, 1998: The Storm Cell Identification and Tracking Algorithm: An enhanced WSR-88D algorithm. *Wea. Forecasting,* **13,** 263–276.

Nuss, W. A., and D. W. Titley, 1994: Use of multiquadric interpolation for meteorological objective analysis. *Mon. Wea. Rev.,* **122,** 1611–1631.

Office of the Federal Coordinator for Meteorological Services and Supporting Research, 2006: Doppler radar meteorological observations: Part C—WSR-88D products and algorithms. Federal Meteorological Handbook No. 11, FCM-H11C-2006, 390 pp.

Perry, J., and A. Biss, 2007: Wind farm clutter mitigation in air surveillance radar. *IEEE Aerospace Electron. Syst. Mag.,* **22,** 35–40.

Poupart, G., 2003: Wind farms impact on radar aviation interests—Final report. QinetiQ Contractor Reps. FES W/14/00614/00/REP and DTI PUB URN 03/1294, 176 pp.

Rinehart, R. E., and E. T. Garvey, 1978: Three-dimensional storm motion detection by conventional weather radar. *Nature,* **273,** 287–289.

Rippa, S., 1999: An algorithm for selecting a good value for the parameter *c* in radial basis function interpolation. *Adv. Comput. Math.,* **11,** 193–210.

Siggia, A., and R. Passarelli, 2005: Gaussian model adaptive processing (GMAP) for improved ground clutter cancel lation and moment calculation. MS-NR:ERAD3-P-00117, Sigmet, Inc., 8 pp.

Sirmans, D., 1993: WSR-88D antenna polarization change. Next Generation Weather Radar Program Technical Rep., Operational Support Facility, Norman, OK, 35 pp.

Spaven Consulting, 2001: Wind turbines and radar: Operational experience and mitigation measures. Edinburgh, United Kingdom, 39 pp.

Vogt, R. J., and Coauthors, 2007: Weather radars and wind farms—Working together for mutual benefit. *Extended Abstracts, WINDPOWER 2007 Conf. and Exhibition,* Los Angeles, CA, AWEA, 15. [Available online at www.roc.noaa.gov/WindFarm/WindPower2007_final_wheader.pdf.]

Webster, D. M., 2005: The effects of wind turbine farms on ATC radar. AWC/WAD/72/665/TRIALS, Air Warfare Center, Waddington, United Kingdom, 48 pp.